

Two-stage MR Image Segmentation Method for Brain Tumors based on Attention Mechanism

Li Zhu, Jiawei Jiang, Lin Lu, Jin Li

March 2023

Abstract: Multimodal magnetic resonance imaging (MRI) can reveal different patterns of human tissue and is crucial for clinical diagnosis. However, limited by cost, noise and manual labeling, obtaining diverse and reliable multimodal MR images remains a challenge. For the same lesion, different MRI manifestations have great differences in background information, coarse positioning and fine structure. In order to obtain better generation and segmentation performance, a coordination-spatial attention generation adversarial network (CASP-GAN) based on the cycle-consistent generative adversarial network (CycleGAN) is proposed. The performance of the generator is optimized by introducing the Coordinate Attention (CA) module and the Spatial Attention (SA) module. The two modules can make full use of the captured location information, accurately locating the interested region, and enhancing the generator model network structure. The ability to extract the structure information and the detailed information of the original medical image can help generate the desired image with higher quality. There exist some problems in the original CycleGAN that the training time is long, the parameter amount is too large, and it is difficult to converge. In response to this problem, we introduce the Coordinate Attention (CA) module to replace the Res Block to reduce the number of parameters, and cooperate with the spatial information extraction network above to strengthen the information extraction ability. On the basis of CASP-GAN, an attentional generative cross-modality segmentation (AGCMS) method is further proposed. This method inputs the modalities generated by CASP-GAN and the real modalities into the segmentation network for brain tumor segmentation. Experimental results show that CASP-GAN outperforms CycleGAN and some state-of-the-art methods in PSNR, SSIM and RMSE in most tasks. In addition, the Dice and Hausdorff95 obtained by AGCMS segmentation are higher than the values corresponding to a single modality, and are close to the values obtained by multiple real modalities, indicating that the method can achieve similar effects as multi-modalities. In summary, the method proposed in this paper can be used as an effective method for clinical diagnosis of brain tumors and has broad application prospects.

Keywords: magnetic resonance imaging, multimodal medical imaging, generative adversarial networks, brain tumor segmentation.

1 Introduction

Medical imaging is a technique to create the visual representation of the human anatomy or function. According to different imaging protocols and modes, their reflection on human tissue characteristics and application are different. The neural network is helpful to understand whether certain tissues of the human body are affected by specific diseases by the classification results and segmentation ones of these medical images. Medical image data show different anatomical

features according to different imaging methods. For example, four modes of the magnetic resonance imaging (MRI)[1], T1 (spin-lattice relaxation), T2 (spin-spin relaxation), Flair (fluid-attenuated inversion recovery) and T1ce (T1-contrast), are commonly used to provide valuable information about the shape, size, location and metabolism of the brain tumors. Different morphologies reflect different biological information and tissue characteristics of the human body. Among them, T1 is beneficial to observe the anatomical structure of brain tissue, such as gray matter and white matter. T2 and Flair highlight the property of the tissue water relaxation, such as whole brain tumors; T1c represents the case occupation of contrast agent in the tumor core[2].

Because different imaging modes can reflect different anatomical characteristics of brain tumors, analysis and diagnosis of the medical image are usually combined with a variety of different MRI modes. Chen et al. decomposed the input modality into the appearance coding representation and the content coding representation, which can enhance the robustness of the multimodal network framework when some modalities are missed[3]. Wang et al. designed a scheme to segment multimodal tumor sub-regions in cascades with the anisotropic convolution[4]. Myronenko described a semantic segmentation network based on the encoder-decoder architecture, which can segment multimodal tumor sub-regions from 3D MRI images[5]. Jiang et al. proposed a new two-stage cascaded U-Net to segment multimodal brain tumors from coarse to fine[6]. Zhang et al. proposed a cross-modal deep feature learning framework to improve the segmentation performance of brain tumors effectively[7]. However, obtaining a complete multimodal MRI image is susceptible to the following factors: (1) During the scanning process, the patient's movement is prone to motion artifacts[8, 9]; (2) Long image scanning time could result miss the optimal diagnosis time[10]; (3) The cost of scanning is expensive[11], causing economic burden to patients. The above factors may lead to incomplete data sets, affecting the quality of the clinical diagnosis and the treatment seriously. Thus, in order to solve the problem of lacking the multimodal data, multimodal MRI image generation task has become one of the focuses in the medical imaging research. But multimodal magnetic resonance imaging does not completely replace the true multimodal magnetic resonance imaging, so there is still a lot of work to be done to achieve true multimodal magnetic resonance imaging performance.

In recent years, generative adversarial networks (GANs)[12] have been proved to be a promising medical imaging generation method[13]. GANs have shown excellent performance in the field of medical images, including medical imaging reconstruction[14, 15], medical imaging classification[16, 17], medical imaging detection[18], medical imaging segmentation[19, 20] and medical imaging denoising[21, 22]. Multimodal medical imaging generation obtains the mapping function from the source image to the target image by learning. On the premise of giving the subject (source domain) image, it can estimate the corresponding target domain image of the same subject accurately. Multimodal medical imaging generation can be divided into two categories: supervised (e.g., conditional generative adversarial networks (cGAN))[23] and unsupervised (e.g., cyclic consensus generative adversarial networks (CycleGAN))[24]. Supervised methods that require paired images have achieved encouraging results in multimodal medical imaging generation recently. For example, the cGAN is used to generate the corresponding mode T1, T2 and Flair from a given mode in an MRI image[25, 26, 27]. However, in most cases, it is very difficult to fully obtain the paired medical images, so the monitoring scheme has certain limitations. Consequently, unsupervised CycleGAN has a broader application prospect in the field of multimodal medical imaging generation. The model can find the mapping relationship between the source image and the target image, which can effectively eliminate the limitation of a pair of corresponding image pairs in the training process. In addition, the CycleGAN also uses cycle consistency loss to preserve key attributes between the input image and the generated image. For example, based on the CycleGAN, Wolterink et al. realized the direct synthesis of

brain CT images from brain MR images without paired data[28]. It is worth noting that in the literature[29], it was emphasized that some unreliable results may be generated during the application of the CycleGAN, resulting in misdiagnosis of the disease. In order to solve this problem, Hiasa et al. improved the CycleGAN network structure by adding gradient consistency loss during the training, then the accuracy of identifying boundaries is raised [30]. While Lilian et al. improved the loss function to solve the existed problem that the gradient disappearance caused by the non-coincidence of the true sample and the generated sample is difficult to train [31]. However, there still exist the problems in the CycleGAN, such as long training time, slow convergence speed and easy to ignore spatial location information. In recent years, generative adversarial networks (GANs)[12] have been proved to be a promising medical imaging generation method[13]. GANs have shown excellent performance in the field of medical images, including medical imaging reconstruction[14, 15], medical imaging classification[16, 17], medical imaging detection[18], medical imaging segmentation[19, 20] and medical imaging denoising[21, 22]. Multimodal medical imaging generation obtains the mapping function from the source image to the target image by learning. On the premise of giving the subject (source domain) image, it can estimate the corresponding target domain image of the same subject accurately. Multimodal medical imaging generation can be divided into two categories: supervised (e.g., conditional generative adversarial networks (cGAN))[23] and unsupervised (e.g., cyclic consensus generative adversarial networks (CycleGAN))[24]. Supervised methods that require paired images have achieved encouraging results in multimodal medical imaging generation recently. For example, the cGAN is used to generate the corresponding mode T1, T2 and Flair from a given mode in an MRI image[25, 26, 27]. However, in most cases, it is very difficult to fully obtain the paired medical images, so the monitoring scheme has certain limitations. Consequently, unsupervised CycleGAN has a broader application prospect in the field of multimodal medical imaging generation. The model can find the mapping relationship between the source image and the target image, which can effectively eliminate the limitation of a pair of corresponding image pairs in the training process. In addition, the CycleGAN also uses cycle consistency loss to preserve key attributes between the input image and the generated image. For example, based on the CycleGAN, Wolterink et al. realized the direct synthesis of brain CT images from brain MR images without paired data[28]. It is worth noting that in the literature[29], it was emphasized that some unreliable results may be generated during the application of the CycleGAN, resulting in misdiagnosis of the disease. In order to solve this problem, Hiasa et al. improved the CycleGAN network structure by adding gradient consistency loss during the training, then the accuracy of identifying boundaries is raised[30]. While Lilian et al. improved the loss function to solve the existed problem that the gradient disappearance caused by the non-coincidence of the true sample and the generated sample is difficult to train[31]. However, there still exist the problems in the CycleGAN, such as long training time, slow convergence speed and easy to ignore spatial location information.

Aiming at the above problems, a Coordinated Attention-Spatial Attention Generative Adversarial Network (CASP-GAN) based on the CycleGAN is proposed for medical imaging generation. While it can greatly accelerate the reasoning speed and reduce the training time, the indicators are improved, or a certain indicator is slightly reduced in exchange for other improvements. In addition, the attention mechanism is introduced, then the segmentation performance of the 3D UNet is improved,. First, CASP-GAN is proposed for multimodal MIR medical imaging generation tasks(T1-to-Flair generation, Flair-to-T1 generation, T1-to-T2 generation and T2-to-T1 generation). Secondly, a multimodal segmentation 3D-CA-UNet method improved by the attention network is proposed, which uses 3D-CA-UNet to segment multimodal MR images. Flair and T2 modes are generated by CASP-GAN and combined with the real T1 mode to segment the entire brain tumor in MR images. What's more, the effectiveness of the proposed method is

verified on the 2020 multimodal brain tumor segmentation challenge (BRATS2020) dataset[32].

The innovations and the contributions of this paper are summarized as follows:

(1) A multimodal medical imaging generation framework CASP-GAN based on the CycleGAN, the CA module and the SP module is proposed. From the ability of extracting the original medical image structure and the detail information, CASP-GAN algorithm can improve the quality of lesion area than other unsupervised algorithms. In terms of the speed of training and reasoning, it can significantly improve the reasoning speed and reduce the network parameters to improve the training speed on the condition of improving or not significantly reducing the indicators.

(2) CASP-GAN introduces the CA module and the SA module to optimize the generator. The size and the shape of the lesion varies from patient to patient and the location is uncertain. The CA module can locate the lesion area more quickly and improve the convergence speed. The SP module can extract the global information of large receptive fields (such as the whole brain) from the spatial scale, which can generate images with more complete structure, more details and better quality. Therefore, the improved generator can better preserve the global background information from the MRI image, and extract the structure, the shape and the connectivity of the lesion faster, thereby obtaining a feature map with higher resolution.

(3) On the basis of 3DUNetCNN, the 3D Coordinate Attention block and the 3D Self Attention block are introduced respectively to optimize the network. The 3D Coordinate Attention block can extracts tumor contour information more efficiently by capturing dependencies between distant pixels; The 3D Self Attention module can use the relationship between pixels adjacent to the lesion to extract tumor details more precisely. On the basis of the network, a MR segmentation network AGCMS integrating CASP-GAN and 3D-CA-NET is further proposed. AGCMS uses the given real modalities and the modality generated by CASP-GAN, which can be used for brain tumor segmentation, and achieves high quantitative performance .

2 Methods

In this paper,an attentional generative multimodal segmentation algorithm AGCMS based on cyclic consistency loss and fusion of four attention mechanisms, is proposed. The method consists of two parts: CASP-GAN (Coordinate Attention Spatial Attention Cycle-consistent Generative Adversarial Networks) and 3D-CA-UNet (3D Coordinate Attention UNet).Firstly,a given 3D image is sliced into 2D images along the z-axis, and then the given 2D images are fed into the CASP-GAN to generate 2D target images; Secondly, the generated 2D image is combined into a complete 3D image along the z-axis. Finally, the given 3D image and the generated 3D image are fed into the segmentation network(3D-CA-UNet) to obtain the final segmentation result. The total algorithm flowchart is shown in Figure 1, where True and False are used to represent the real image and the generated image.

2.1 Multi-Modality Generation

The CASP-GAN model proposed in this paper can be used for multimodal medical image generation. The CASP-GAN method can learn the mapping relationship between the source modal image and the target modal image. On the basis of the CycleGAN, SP module is added to the generator to enhance the extraction ability of the location feature. The 9-layer standard residual module used in CycleGAN has the disadvantages of large amount of calculation, slow reasoning speed and slow convergence speed. In the proposed CASP-GAN, the CA module is used to replace the residual module in the original network, which greatly reduces the number of parameters and accelerates the convergence speed without losing the quality of the generated

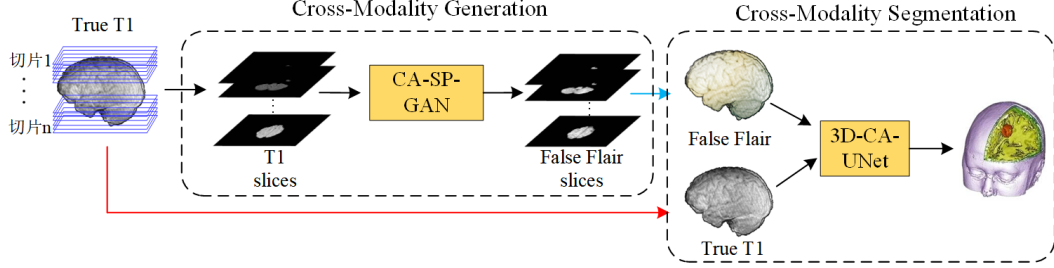


Figure 1: AGCMS flowchart

image. When the input modal image is x , the output image \hat{y} can be obtained by the generator $G_{x \rightarrow y}$. Then, \hat{y} can be obtained through the generator $G_{y \rightarrow x}$, where \hat{y} is the required target-modality image, and \hat{x} is the cyclically generated image; by analogy, when the input is a modal image y , the desired target modal image \hat{x} is obtained. The obtained image \hat{y} is generated circularly. The specific structure is shown in Figure 2.

2.1.1 Generator based on Coordinate Attention

Studies have shown that channel attention can significantly improve the performance of the model, but channel attention often ignores the location information which is important for generating space. In order to solve this problem, Hou et al.[33] proposed Coordinate attention (CA). Therefore, the Coordinate attention module is applied to the CASP-GAN generator in this paper. As shown in Figure 3, it is composed of cross attention embedding, cross attention generation and information fusion. A comparison with the standard residual module network architecture is shown in Figure 3.

Location information extraction has a crucial impact on the image generation model of pixel-level brain tumor. By decomposing the channel attention into two 1D feature encoding processes that can aggregate features along different directions, long-range dependence can be captured and accurate location information can be extracted along two spatial directions at the same time, then they can be encoded to form a feature map that is sensitive to both direction and position. It can complementarily represent the feature information of the region of interest of the input image.

Woo et al.[34] proposed that the CBAM performs adaptive feature optimization by inferring the attention feature map in the space and the channel respectively, and multiplying the attention feature map with the input feature map. In the spatial attention, average pooling and maximum pooling are used to extract network attention map. Average pooling can well retain the characteristics of the overall data, highlighting the background information; maximum pooling can better preserve the texture features. However, for brain tumor data, since the original image data is a single channel after slicing, it is difficult to produce a substantial effect using the channel attention, and the adaptive optimization of spatial dimension is indispensable. SP module network architecture is shown in Figure 4.

The input feature map is simultaneously max-pooled and mean-pooled in the channel dimension to generate two 2D feature maps $\mathbf{F}_{\text{avg}}^s \in \mathbb{R}^{1 \times H \times W}$ and $\mathbf{F}_{\text{max}}^s \in \mathbb{R}^{1 \times H \times W}$, then the two feature maps are merged and are performed by the feature fusion through a 7×7 convolution. The larger receptive field can provide wider feature information. Finally, the weight map is generated by the sigmoid operation and superimposed back to the original input feature map to

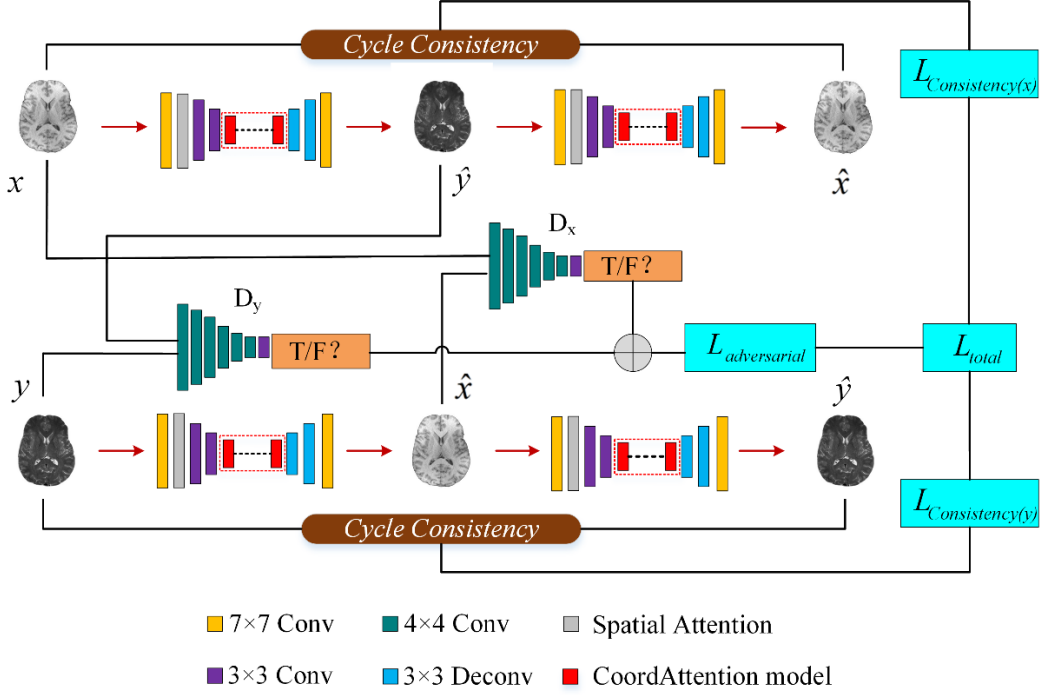


Figure 2: Framework of the CASP-GAN. When the input modal image is x , an image \hat{y} is obtained by the generator $G_{x \rightarrow y}$. Then, the image \hat{y} is fed into the generator $G_{y \rightarrow x}$ to get the image \hat{x} , where the image \hat{y} is the required target modality image and \hat{x} is the cyclically generated image; Similarly, when the input is an image y , the obtained \hat{x} is the required target-modality image and the obtained \hat{y} is the cyclic generated image.

enhance the target area. The final results are as follows:

$$\begin{aligned}
 \mathbf{M}_s(\mathbf{F}) &= \sigma \left(f^{7 \times 7} ([\text{AvgPool}(\mathbf{F}); \text{MaxPool}(\mathbf{F})]) \right) \\
 &= \sigma \left(f^{7 \times 7} ([\mathbf{F}_{\text{arg}}^s; \mathbf{F}_{\text{max}}^s]) \right)
 \end{aligned} \tag{1}$$

where $f^{7 \times 7}$ represents the sigmoid function, which is the convolution of the size of 7×7 .

2.2 Multi-Modality Segmentation

In this paper, 3D-Attention-UNet is proposed model for cross-modality medical image segmentation, which consist of encoder, decoder, and jump connection. Building on top of 3D UNetCNN, 3D Self-attention and 3D Coordinate attention are introduced in the jump connection to increase the weight of effective information and reduce redundant information. Firstly, the image output by the encoder is passed through the corresponding attention block, it is stitched with the output image after upsampling through jump connection. Secondly, the stitched image is fed into the decoder; Finally, the image through the decoder is passed through a $1 \times 1 \times 1$ convolutional layer and a softmax activation function layer to obtain a segmentation result image consistent with the size of the input image. The proposed 3D-attention-UNet framework is shown in Figure 5. In this paper, 3D Self Attention and 3D Coordinate Attention at jump connections is introduced to form two different networks respectively: 3D-SA-UNet and 3D-CA-UNet.

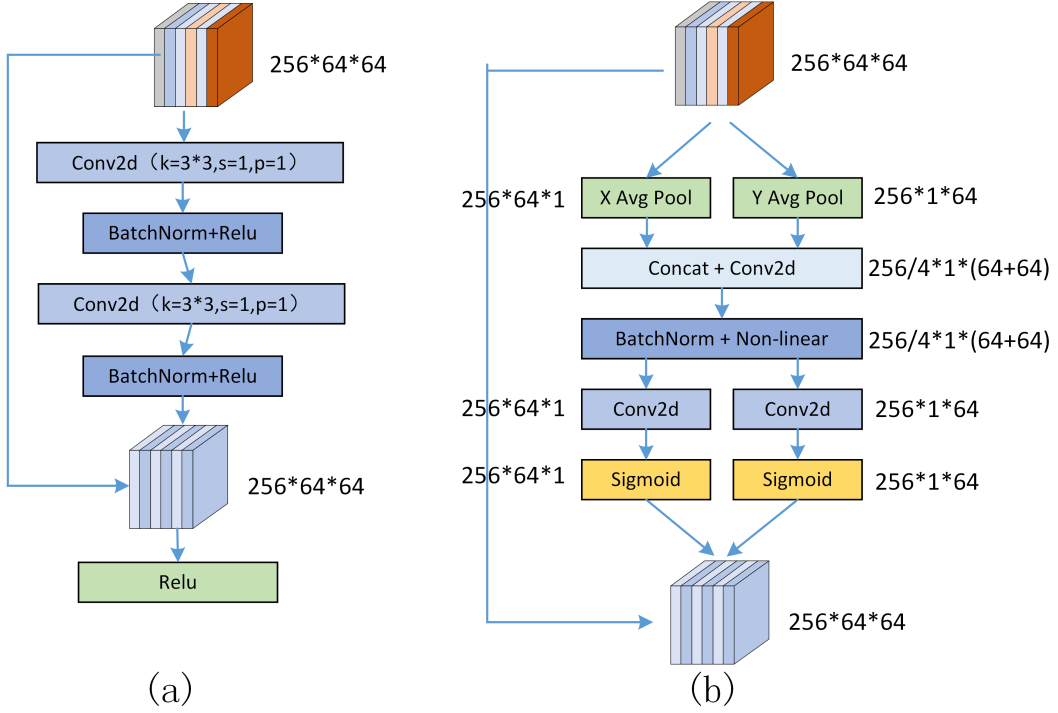


Figure 3: CA block network architecture diagram.(a) is the residual module in the original network, (b) is the Coordinate attention block

2.2.1 3D Self Attention

The Self Attention block was originally applied to natural language processing to effectively establish long-term dependencies between sentences. In this paper, the extended 3D Self Attention block is introduced to the jump connection of the segmentation network for brain tumor segmentation, which can use the relationship between pixels adjacent to the lesion to extract tumor details more precisely. The proposed 3D Self Attention framework is shown in Figure 5(b).

The calculation process of the 3D Self attention module is as follows: Firstly, a given 3D feature map $F \in R^{C \times H \times W \times D}$ is passed through three convolutional layers with the size of $1 \times 1 \times 1$ respectively to obtain $Q(x) \in R^{C \times H \times W \times D}$, $K(x) \in R^{C \times H \times W \times D}$ and $V(x) \in R^{C \times H \times W \times D}$. Secondly, to obtain the attention feature map, the transposed $Q(x)$ is multiplied by $K(x)$ and pass it through softmax; Finally, the attention feature map is multiplied by $V(x)$ to obtain the self-attention feature map. The final output is as follows.

$$\text{Attention}(Q, K, V) = \text{softmax} \left(\frac{QK^T}{\sqrt{d_k}} \right) V \quad (2)$$

2.2.2 3D Coordinate Attention

Based on the CA block in CASP-GAN, extended 3D Coordinate Attention block is introduced to the jump connection of the segmentation network, which can extracts tumor contour information more efficiently by capturing dependencies between pixels at a distance. The proposed

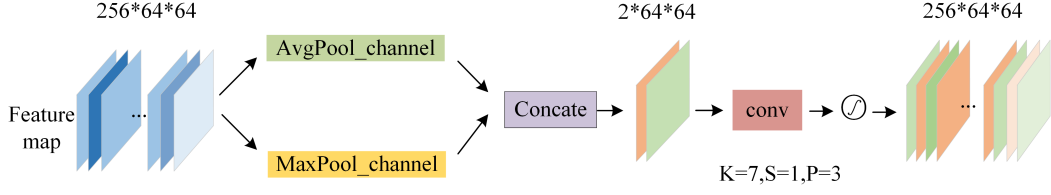


Figure 4: SP module network architecture diagram

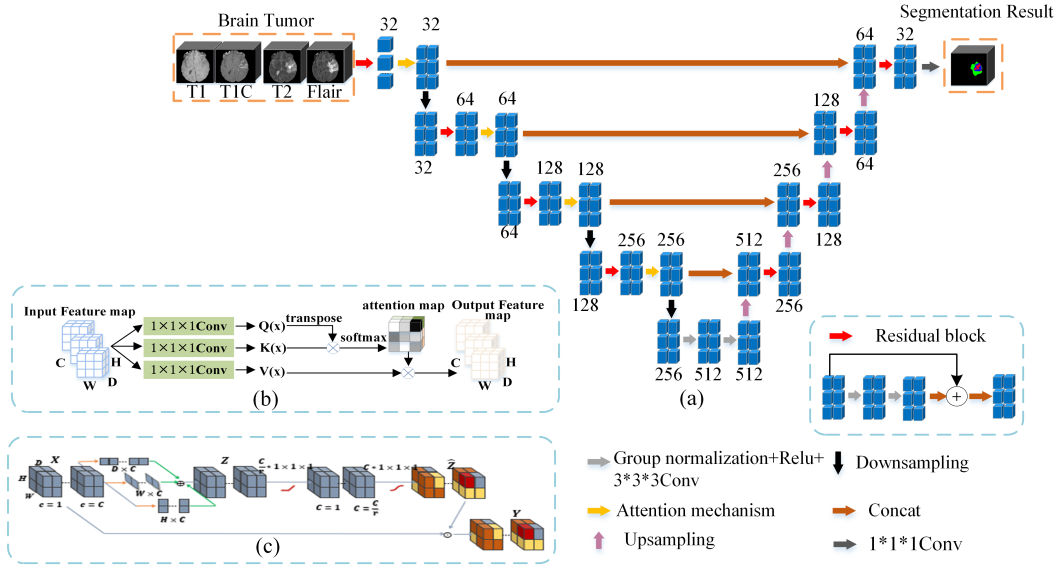


Figure 5: 3D-Attention-UNet algorithm framework diagram

3D Coordinate Attention framework is shown in Figure 5(c).

Compared with the CA block, we factorize the global pooling of the 3D Coordinate Attention block into 1D feature encoding operations along three different directions.

Firstly, given the input 3D feature map $F \in R^{C \times H \times W \times D}$, we use three spatial extents of pooling kernels $(H, 1, 1)$, $(1, W, 1)$ or $(1, 1, D)$ to encode each channel along the horizontal, vertical and depth directions. Thus, the output of the c -th channel at height h can be defined as:

$$z_c^h(h) = \frac{1}{W \times D} \sum_{j=1}^W \sum_{k=1}^D x_c(h, j, k) \quad (3)$$

Similarly, the output of the c -th channel at width w can be defined as:

$$z_c^w(w) = \frac{1}{H \times D} \sum_{i=1}^H \sum_{k=1}^D x_c(i, w, k) \quad (4)$$

The output of the c -th channel at depth d can be defined as:

$$z_c^d(d) = \frac{1}{H \times W} \sum_{i=1}^H \sum_{j=1}^W x_c(i, j, d) \quad (5)$$

Secondly, given the aggregated feature maps produced by Eqn. 3, Eqn. 4 and Eqn. 5, we concatenate them and then send them to a shared $1 \times 1 \times 1$ convolutional transformation function F_1 , we can be defined as:

$$f = \delta(F_1([z^h, z^w, z^d])) \quad (6)$$

After the Sigmoid activation function, the following result is obtained as:

$$g^h = \sigma(F_h(f^h)) \quad (7)$$

$$g^w = \sigma(F_w(f^w)) \quad (8)$$

$$g^d = \sigma(F_d(f^d)) \quad (9)$$

Finally, the g^h, g^w and g^d are expanded and used as attention weights, the result of our coordinate attention block can be defined as:

$$y_c(i, j, k) = x_c(i, j, k) \times g_c^h \times g_c^w \times g_c^d \quad (10)$$

3 Experiments and Results

3.1 Datasets

This paper uses the BraTS2020[32] data set, including multimodal training data of 369 cases and multimodal verification data of 125 cases. The data of each case contains four modalities : T1, T1ce, T2 and Flair. All data has been skull stripping, linear alignment. The size is $240 \times 240 \times 155$. Four modal images in the data set are selected to verify the effectiveness of the proposed multimodal medical image generation algorithm. The training data are randomly divided into three parts: PartA (164 cases), PartB (164 cases) and PartC(41 cases). PartA is used as the training data set of the generation model, PartB is used as the training data set of the segmentation model, and PartC is used as the common test set of the generation model and the segmentation model.

For CASP-GAN, the cross-sectional slices of 26-125 layers(100 layers in total) of each case were selected as the original data. The size of the slice image is filled to zero around. There are 16400($64 \times 100 = 16400$) images in the training dataset and 4100($41 \times 100 = 4100$) images in the test dataset.

For 3D-CA-UNet, the validity of the proposed 3D-SA-UNet and 3D-CA-UNet models was first tested using 66 cases in the BraTS2020 validation set, and the 3D-CA-UNet model was selected as the segmentation model. The 2D image generated by CASP-GAN is synthesized into a complete 3D image along the cross section and then input into the segmentation model as False mode. The original data of BRATS2020 is used as True modal input. The 3D-CA-UNet training set has 164 images in 3D format for each modality, and the test set has 41 images in 3D format for each modality. All images are normalized by mean and standard deviation.

3.2 Implementation Details

In the medical image generation experiment, the learning rate is set to 0.0002, epoch is set to 40, and the batch size is 1. The training process uses the Adam optimizer[35] and the attenuation factor is set to. In addition to the performance evaluation of the CASP-GAN algorithm proposed in this paper, the performance comparison with the existing similar algorithms is also performed, which are DiscoGAN[36], UNIT[37] and CycleGAN[24]. The hardware and software environment used in this experiment is shown in Table 1.

Table 1: Software environment and hardware configuration in the experiment.

Software/Hardware	Parameters
GPU	NVIDIA TITAN Xp
System	Ubuntu 16.04 LTS
Programming Language	Python 3.7
Machine Learning Platform	Pytorch
Parallel Computing Platform	CUDA 10.0

3.3 Results

3.3.1 Multi-Modality Generation

Evaluation Measures. In this paper, three image evaluation indexes are used to evaluate the performance of the CASP-GAN and other methods, namely PSNR[38], SSIM[39] and RMSE. Generation Result. The generation performance of the CASP-GAN is evaluated on four tasks in this paper: (1) T1 is used to generate Flair; (2) Flair is used to generate T1; (3) T1 is used to generate T2; (4) T2 is used to generate T1. And the proposed method is compared with DiscoGAN [36], UNIT[37] and CycleGAN[24]. In addition, ablation experiments are performed on the CASP-GAN.

The T1-Flair dataset are trained and evaluated the performances of the experiment generating Flair images from T1 images and the experiment generating T1 images from Flair images, and comparative experiments with only the SP module added and only the CA module replaced are also included. It can be seen from Table 2:

1. In the T1 to Flair generation experiment, the SSIM value of the CASP-GAN proposed in this paper is 0.876 ± 0.038 , which reaches the optimal value. In terms of the PSNR value (23.451 ± 2.742), although it is slightly lower than the CycleGAN algorithm, it is higher than the other two comparison algorithms. Moreover, RMSE value (18.028 ± 5.943) is consistent with CycleGAN algorithm, but still better than the other two algorithms.
2. In the Flair to T1 generation experiment, three quantitative image evaluation indexes PSNR, SSIM and RMSE of the CASP-GAN are 23.940 ± 2.838 , 0.909 ± 0.031 and 15.273 ± 5.557 , respectively. These three indicators are superior to the other three comparison algorithms.

It can be observed from Figure 6 that in the T1 to Flair generation task, the average value of the proposed CASP-GAN on the SSIM index is optimal, and the average value of the RMSE index is the same as that of the CycleGAN. In addition, the fluctuation range of SSIM index is significantly reduced, which shows an excellent performance.

In Figure 7, it can be observed that in the Flair to T1 generation task, the average value of the proposed CASP-GAN in PSNR, SSIM and RMSE is optimal. In addition, the fluctuation range of PSNR, SSIM and RMSE is significantly reduced, and the performance is excellent.

Figure 8 shows the attention heat maps generated by the Grad-CAM network using the case brain tumor sections (a),(b),(c)and(d) under different algorithms, which can represent the attention areas to the medical images of different algorithm networks. Blue represents the area of no concern and red represents the area of concern. It can be observed from the figure that due to the existence of the CA module and the SP module, the CASP-GAN algorithm can save more attention areas than the original CycleGAN algorithm, so as to better extract the context details of the image and generate better quality target source images.

Table 2: Quantitative evaluation results(mean \pm standard deviation) of different generating algorithms on T1 to Flair task and Flair to T1 task in the BraTS2020 dataset. Numbers in bold indicate the best result.

	Methods	PSNR	SSIM	RMSE
T1 to Flair	DiscoGAN	19.255 \pm 3.229	0.796 \pm 0.065	29.784 \pm 11.289
	UNIT	22.477 \pm 3.286	0.858 \pm 0.050	20.657 \pm 8.498
	CycleGAN	23.940 \pm 2.839	0.876 \pm 0.040	18.028 \pm 5.943
	CycleGAN + SP	23.705 \pm 2.988	0.875 \pm 0.040	17.703 \pm 6.631
	CycleGAN + CA	23.292 \pm 2.737	0.873 \pm 0.040	18.332 \pm 5.759
	CASP - GAN	23.451 \pm 2.742	0.876 \pm 0.038	18.028 \pm 5.943
Flair to T1	DiscoGAN	21.076 \pm 2.954	0.849 \pm 0.053	23.876 \pm 8.349
	UNIT	223.627 \pm 3.393	0.888 \pm 0.040	18.149 \pm 7.478
	CycleGAN	24.648 \pm 2.993	0.892 \pm 0.043	15.838 \pm 5.580
	CycleGAN + SP	24.743 \pm 2.907	0.904 \pm 0.034	15.640 \pm 5.584
	CycleGAN + CA	24.776 \pm 2.856	0.899 \pm 0.036	15.561 \pm 5.557
	CASP - GAN	24.940 \pm 2.838	0.909 \pm 0.031	15.273 \pm 5.557

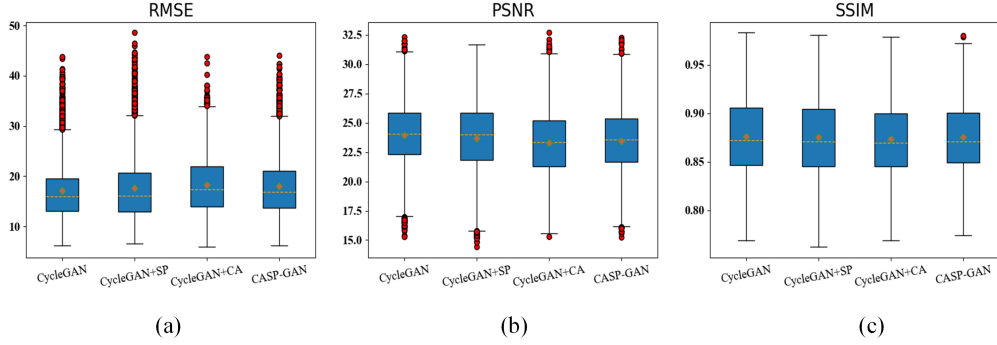


Figure 6: T1 to Flair box plots of different algorithms based on BraTS2020: (a) PSNR, (b) SSIM,

The 114th slice of the 71st case, the 71st slice of the 156th case, the 73rd slice of the 171st case and the 80th slice of the 251st case are abbreviated as case (a), case (b), case (c) and case (d), respectively. Compared with the original CycleGAN, the proposed CASP-GAN generation algorithm uses two different key modules: the SP module and the CA module. Therefore, in order to verify the role of each module used, ablation experiments are performed based on the generation tasks of T1 to Flair and Flair to T1, including the following four models:

- The original CycleGAN ;
- Add SP module on the basis of a) ;
- Replace with CA module on the basis of a) ;
- Add the SP module and replace with the CA module on the basis of a), that is CASP-GAN proposed in this paper.

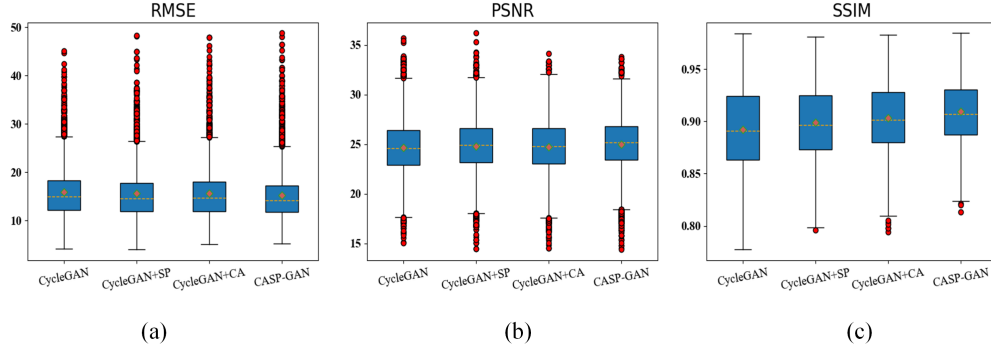


Figure 7: Flair to T1 box plot of different algorithms based on BraTS2020: (a) PSNR, (b) SSIM, (c) RMSE

The results of the ablation experiment are shown in Table 3. From the PSNR, SSIM and RMSE indexes in the T1 to Flair results, it can be seen that adding the SP module alone improves the RMSE index, and replacing with the CA module and adding the SP module make the SSIM index optimal. The best model in the Flair to T1 experimental result is the d) model. It can be observed from the PSNR, SSIM and RMSE indicators that the two key modules used in this algorithm have different degrees of improvement in the performance of the generated model.

Table 3: CASP-GAN Ablation Experiment Based on T1 to Flair and Flair to T1 Generation Tasks

Case	Tasks	(SP)	(CA)	PSNR	SSIM	RMSE
a)	T1 to Flair	✗	✗	23.940 ± 2.839	0.876 ± 0.040	18.028 ± 5.943
b)		✓	✗	23.705 ± 2.988	0.875 ± 0.040	17.703 ± 6.631
c)		✗	✓	23.292 ± 2.737	0.873 ± 0.040	18.332 ± 5.759
d)		✓	✓	23.451 ± 2.742	0.876 ± 0.038	18.028 ± 5.943
a)	T1 to Flair	✗	✗	24.648 ± 2.993	0.892 ± 0.043	15.838 ± 5.580
b)		✓	✗	24.743 ± 2.907	0.904 ± 0.034	15.640 ± 5.584
c)		✗	✓	24.776 ± 2.856	0.899 ± 0.036	15.561 ± 5.557
d)		✓	✓	24.940 ± 2.838	0.909 ± 0.031	15.273 ± 5.557

For T1 to Flair task, the error comparison between the image generated by different algorithms and the original input image T1 is shown in Figure 9. Compared with the original CycleGAN generation algorithm, the image quality generated by the CASP-GAN generation algorithm is better and more similar to the original input image T1, indicating that the replaced CA module and the added SP module can extract the details of the original input image more effectively, and perform better in generating similar images.

The T1-T2 dataset are trained and evaluated the performances of the experiment generating T2 images from T1 images and generating T1 images from T2 images. The performance of the DiscoGAN, the UNIT and the CycleGAN are displayed. It can be seen from Table 4:

1. In the T1 to T2 generation experiment, the SSIM value and the RMSE value of the proposed CASP-GAN are 24.815 ± 2.752 and 15.438 ± 5.343 , respectively, which both reach the

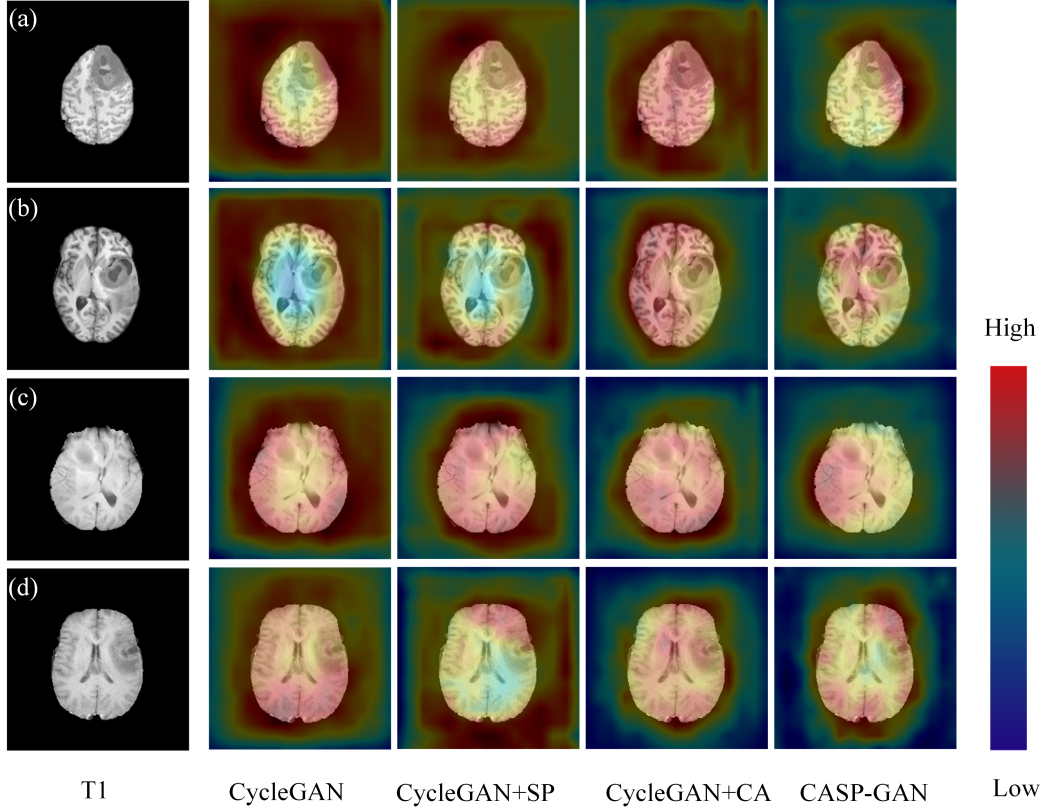


Figure 8: Comparison of attention heat maps of different algorithms

optimal values. In terms of the SSIM value (0.911 ± 0.033), although it is slightly lower than the CycleGAN algorithm, it is higher than the other two comparison algorithms.

2. In the T2 to T1 generation experiment, the SSIM value and the RMSE value of the proposed CASP-GAN are 24.297 ± 3.292 and 16.763 ± 6.979 , respectively, which both reach the optimal values. As for the SSIM value (0.911 ± 0.050), it is slightly lower than the CycleGAN algorithm, but it is higher than the other two comparison algorithms.

The parameter is used to describe the size of the model. The formula of the convolution layer parameter is defined as follows:

$$\text{params} = C_0 \times (k_w \times k_h \times C_i + 1) \quad (11)$$

where C_0 represents the number of output channels, C_i represents the number of input channels, k_w and k_h are the sizes of the convolution kernels, respectively. The amount of calculation is used to describe the length of the execution of the model. The formula for the calculation of the convolution layer is displayed as follows:

$$\text{flops} = [C_i \times k_w \times k_h + (C_i \times k_w \times k_h - 1) + 1] \times W \times H \times C_0 \quad (12)$$

where $C_i \times k_w \times k_h$ is the calculation amount of the multiplication operation of a convolution, $C_i \times k_w \times k_h - 1$ is the calculation amount of the addition operation of a convolution, $+1$ is the bias term, W and H are the length and the width of the feature map, respectively.

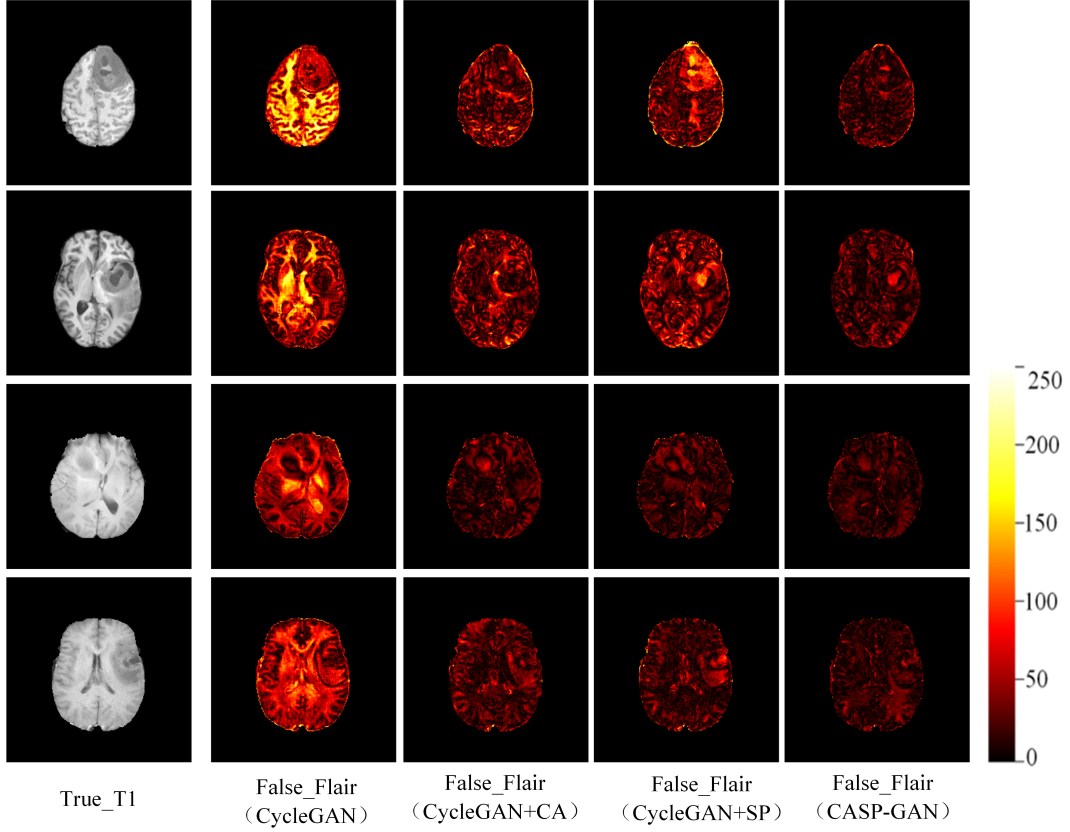


Figure 9: Comparison of error plots for T1→Flair ablation experiments

Table 4: Comparison of different algorithm performance indexes of T1 to T2 and T2 to T1 generation tasks based on BraTS2020 data set.

	Methods	PSNR	SSIM	RMSE
T1 to T2	DiscoGAN	19.255 ± 3.229	0.796 ± 0.065	29.784 ± 11.289
	UNIT	22.477 ± 3.286	0.858 ± 0.050	20.657 ± 8.498
	CycleGAN	24.626 ± 2.943	0.917 ± 0.033	15.888 ± 5.829
	CASP – GAN	24.815 ± 2.752	0.911 ± 0.033	15.438 ± 5.343
T2 to T1	DiscoGAN	21.076 ± 2.954	0.849 ± 0.053	23.876 ± 8.349
	UNIT	23.627 ± 3.393	0.888 ± 0.040	18.149 ± 7.478
	CycleGAN	23.898 ± 3.652	0.917 ± 0.046	17.869 ± 8.404
	CASP – GAN	24.297 ± 3.292	0.911 ± 0.050	16.763 ± 6.979

It can be seen from Table 5 that compared with the CycleGAN, the CASP-GAN proposed in this paper can significantly reduce the amount of calculation and parameters, and the computational complexity is lower.

Table 5: Comparison results of calculation amount and parameter amount of different algorithm.

Methods	flops	Params	FPS
CycleGAN	41534.16M	7.83M	8.7
CASP – GAN	13535.17M	0.80M	14.8

3.3.2 Cross-Modality Segmentation

Evaluation Measures. In this paper, Dice, Sensitivity, Specificity and Hausdorff95 are used to evaluate the segmentation results, and the results of the four segmentation indicators are obtained by uploading the prediction labels to the BRATS2020 official website (<https://ipp.cbica.upenn.edu/login>). The values of Dice, Sensitivity and Specificity are between 0 and 1, and the value range of Hausdorff95 is 0-100. The higher the Dice and the lower the Hausdorff95, the better the segmentation results.

Segmentation Result. (1) In this paper, the segmentation performance of the 3D-SA-UNet and the 3D-CA-UNet is evaluated by using 66 cases from the BraTS2020 Validation dataset. The results of the 3D-SA-UNet and the 3D-CA-UNet are compared with three state-of-the-art methods, including 3D UNet[40], nn-UNet[41] and 3DUNetCNN[42], where the 3D-CA-UNet is chosen as the segmentation model. (2) In MR images, the T1 modality facilitates the observation of the gray matter and the white matter of the brain, and the modalities of Flair and T2 are favorable to locate tumors. It is noteworthy that the T1 modality is the fastest and the easiest modality to obtain. Therefore, the modalities of Flair and T2 are generated by the true T1 modality, then they both are added into the true T1 modality respectively for the segmentation of the whole brain tumor.

Table 6 shows the segmentation performance of the proposed 3D-SA-UNet, the 3D-CA-UNet and the other compared algorithms on the BraTS2020 Validation set. As can be seen from Table 6, the Dice of WT and TC of the 3D-SA-UNet and the Hausdorff95 are better than the 3D UNet, the 3DUNetCNN. what’s more, the Dice of TC of the 3D-SA-UNet is better than the one of the nnU-Net. It can be seen that the 3D-SA-UNet algorithm has good segmentation performance in WT and TC. The 3D CA-UNet algorithm is slightly lower than that of 3D-SA-UNet in the segmentation performance of WT and TC, but it makes up for the shortcomings of 3D-SA-UNet in ET segmentation. Consequently, the 3D-CA-UNet algorithm has better comprehensive segmentation performance. In this paper, the 3D-CA-UNet is chosen as a segmentation network to verify the validity of the generation algorithm.

Table 6: Quantitative evaluation results of the 3D-SA-UNet and the 3D-CA-UNet compared with the nn-UNet, the 3D UNet and the 3DUNetCNN on BraTS2020 Validation set. (Numbers in bold indicate the best result. Numbers with underline indicate the better result.)

Methods	Dice			Hausdorff95		
	WT	TC	ET	WT	TC	ET
nn – UNet	0.907	0.817	0.736	4.307	7.029	35.788
3D UNet	0.884	0.763	0.734	6.543	17.623	34.525
3DUNetCNN	0.897	0.826	0.719	8.000	10.031	36.525
3D – SA – UNet	0.900	0.836	0.685	4.858	6.678	48.350
3D – CA – UNet	0.898	0.831	0.716	5.559	6.801	39.483

Figure 10 show the qualitative comparisons between the proposed 3D-SA-UNet, the 3D-CA-UNet and the 3DUNetCNN on the BraTS2020 dataset. As shown in Figure 10 (a), the proposed two algorithms achieved good segmentation in the whole, and it can be seen from the yellow dotted circle in Figure 10 (a*) that in the challenge of discrete small lesions, 3D Coordinate Attention U-Net can still segment small lesions better than other algorithms, and the segmentation is more obvious at the boundary; as shown in Figure 10 (b), the two proposed algorithms have improved the segmentation performance in the TC of the tumor, and it can be seen from the yellow dotted circle of Figure 10 (b) (b*) that the 3D-CA-UNet has a greater segmentation advantage in the tumor necrotic region; it can be seen from Figure 10 (c) and (c*) that the 3D-CA-UNet has a good segmentation performance on these lesion areas which are in irregular shape and disconnected.

Figure 11 shows the attention heat maps of the case brain tumor sections (a), (b) and (c) under different segmentation algorithms, which can represent the attention areas to the medical images of different networks. Blue represents the area of no concern and red represents the area of concern. It can be observed that due to the existence of the 3D Coordinate Attention block and the 3D Self Attention block, the 3D-SA-UNet and the 3D-CA-UNet can focus more areas of brain tumors than the original 3DUNetCNN algorithm, then the segmentation accuracy of brain tumors can be improved.

Table 7 shows the quantitative evaluation results on the T1-T2 dataset of the BraTS2020. As can be seen from Table 7, the Dice (0.914), Sensitivity (0.897), Specificity (0.999), and Hausdorff95 (5.523) of AGCMS are superior to the segmentation results using only the true modalities of T1 and Flair, and are close to the ones from the true modalities (True T1+True T2+ True Flair). The results show that the false T2 image generated by CASP-GAN carries some details of the brain tumor region and can replace the real T2 for the segmentation of the whole brain tumor.

Table 7: Quantitative evaluation results of the segmentation results on the T1-T2 dataset. True T1+True Flair indicates the 3D-CA-UNet where the inputs are true T1 images and true T2. AGCMS (True T1+True T2+False T2) indicates the proposed method where the inputs are true T1, true Flair and false T2 generated by CASP-GAN. True T1+True T2+True Flair indicates the 3D-CA-UNet where the inputs are true T1 images, true T2 images and true Flair images. Numbers in bold indicate the best result.

Methods	Dice	Sensitivity	Specificity	Hausdorff95
TrueT1 + TrueFlair	0.909	0.887	0.998	6.018
AGCMS	0.914	0.897	0.999	5.523
TrueT1 + TrueT2 + TrueFlair	0.919	0.916	0.998	5.686

Table 8 shows the quantitative evaluation results on the T1-Flair dataset of the BraTS2020. As can be seen from Table 8, the Dice (0.892), Sensitivity (0.883), Specificity (0.999), and Hausdorff95 (6.362) of AGCMS are superior to the segmentation results by using only the true modalities of T1 and T2, respectively, and are close to the segmentation results with the true modalities (True T1+True T2+True Flair). Overall, the False Flair generated by CASP-GAN also can help the segmentation performance on the whole brain tumors.

3.4 Conclusion

In this paper, based on the attention mechanism, a multimodal generation countermeasure network CASP-GAN is designed, and it uses 3D-Unet to split the network for verification. First of all, combining the spatial attention network with the coordinated attention network replaced

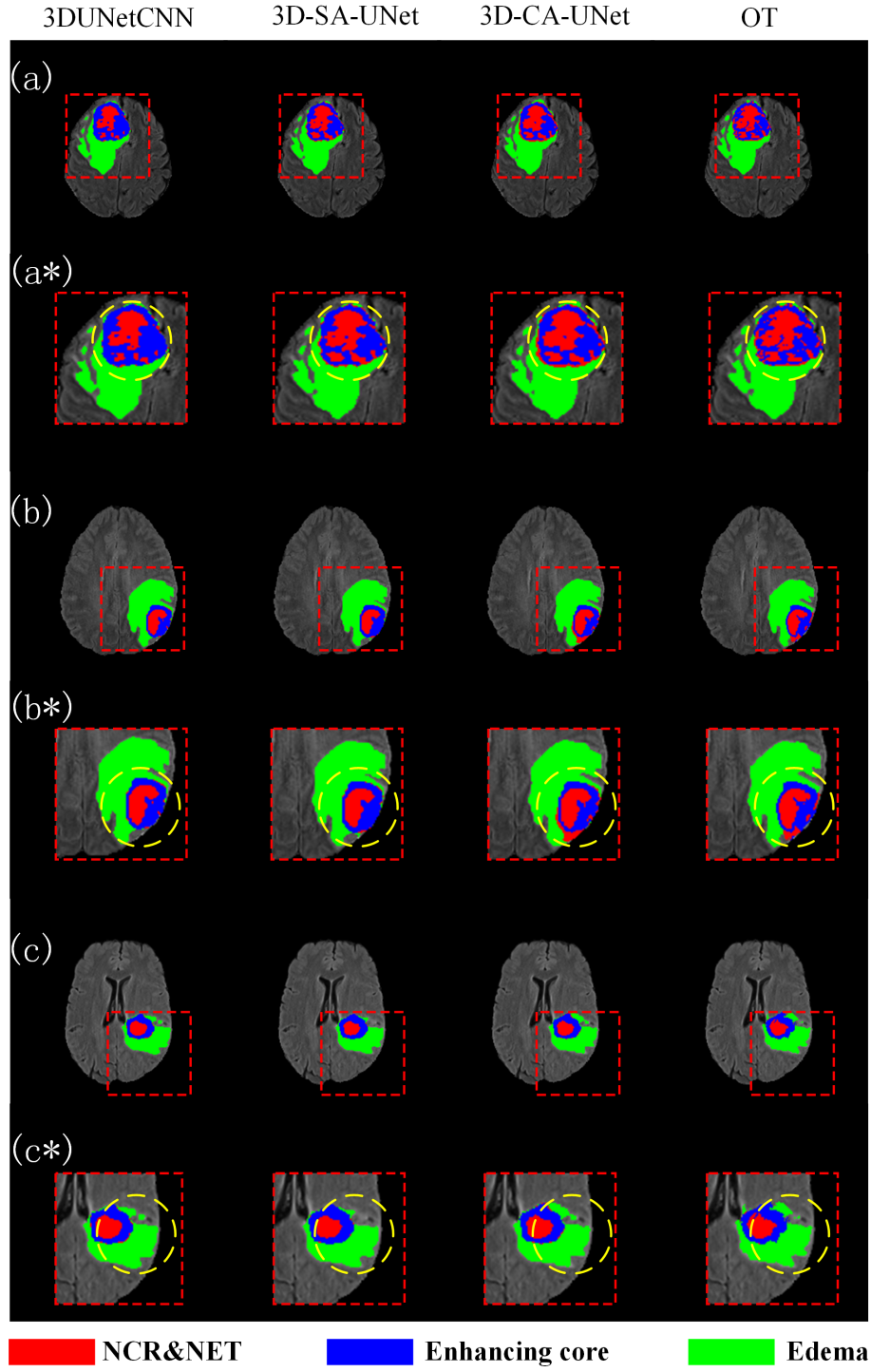


Figure 10: Qualitative comparisons of the 3D-SA-UNet, the 3D-CA-UNet with the 3DUNetCNN. (a), (b), and (c) are normal-sized brain images, respectively; (a*), (b*), and (c*) are the details of brain tumors in (a), (b), and (c), respectively.

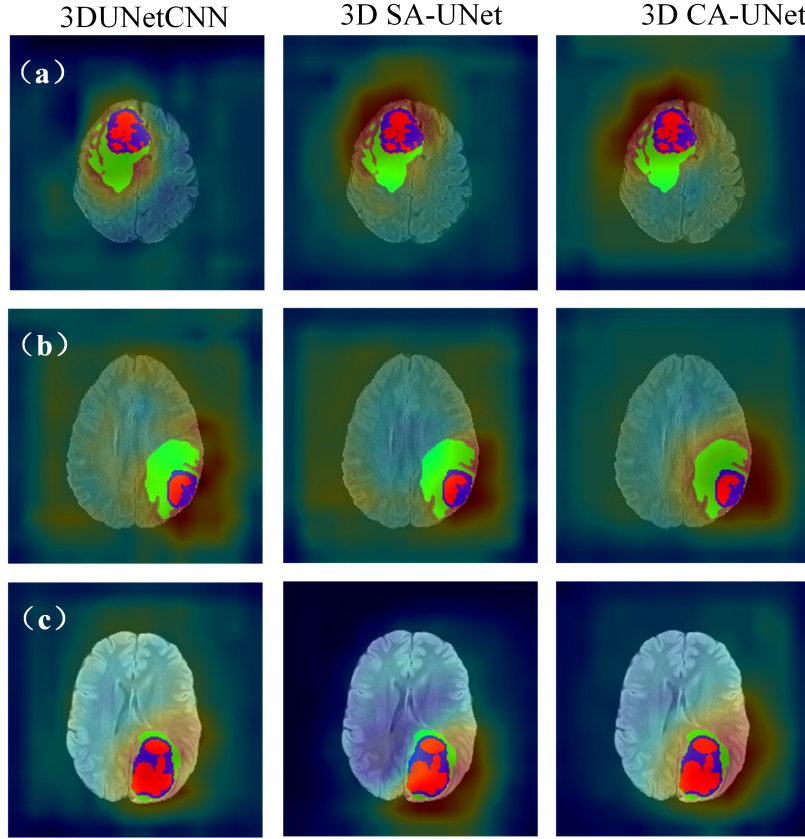


Figure 11: Comparison of attention heat maps of different algorithms on BraTS2020.

Table 8: Quantitative evaluation results of the segmentation results on the T1-Flair dataset. True T1+True T2 indicates 3D-CA-UNet where inputs are true T1 images and true T2. AGCMS (True T1+ TrueT2+False T2) indicates the proposed method where inputs are true T1, true T2 and false Flair generated by CASP-GAN. True T1+True T2+TrueFlair indicates 3D-CA-UNet where inputs are true T1 images, true T2 images and True Flair. Numbers in bold indicate the best result.

Methods	Dice	Sensitivity	Specificity	Hausdorff9
TrueT1 + TrueT2	0.882	0.837	0.998	6.622
AGCMS				
(True T1+True T2+False Flair)	0.892	0.883	0.999	6.362
TrueT1 + TrueT2 + TrueFlair	0.919	0.916	0.998	5.686

by the residual module is conducive to extracting more details and texture features. At the same time, the amount of the computation time and the computation time are greatly reduced, and the required memory capacity is also greatly lowered. Secondly, in the four generation tasks from T1 to T2, T2 to T1, T1 to Flair, and Flair to T1, PSNR, SSIM, RMSE quantitative evaluation indicators and visual qualitative results are better than other comparison algorithms.

Finally, in the segmentation task, the proposed CASP-GAN can segment brain tumors more completely, and the segmentation performance is better than that of dual-mode input model, and the segmentation performance is similar to that when the input is real modal image. Therefore, the proposed CASP-GAN has a promising application in multimodal medical image generation tasks.

References

- [1] K.-L. Tseng, Y.-L. Lin, W. Hsu, *et al.*, “Joint sequence learning and cross-modality convolution for 3d biomedical segmentation,” in *Proceedings of the IEEE conference on Computer Vision and Pattern Recognition*, 6393–6400 (2017).
- [2] U. Baid, S. Ghodasara, S. Mohan, *et al.*, “The rsna-asnr-miccai brats 2021 benchmark on brain tumor segmentation and radiogenomic classification,” *arXiv preprint arXiv:2107.02314* (2021).
- [3] C. Chen, Q. Dou, Y. Jin, *et al.*, “Robust multimodal brain tumor segmentation via feature disentanglement and gated fusion,” in *Medical Image Computing and Computer Assisted Intervention–MICCAI 2019: 22nd International Conference, Shenzhen, China, October 13–17, 2019, Proceedings, Part III 22*, 447–456, Springer (2019).
- [4] G. Wang, W. Li, S. Ourselin, *et al.*, “Automatic brain tumor segmentation using cascaded anisotropic convolutional neural networks,” in *Brainlesion: Glioma, Multiple Sclerosis, Stroke and Traumatic Brain Injuries: Third International Workshop, BrainLes 2017, Held in Conjunction with MICCAI 2017, Quebec City, QC, Canada, September 14, 2017, Revised Selected Papers 3*, 178–190, Springer (2018).
- [5] A. Myronenko, “3d mri brain tumor segmentation using autoencoder regularization,” in *Brainlesion: Glioma, Multiple Sclerosis, Stroke and Traumatic Brain Injuries: 4th International Workshop, BrainLes 2018, Held in Conjunction with MICCAI 2018, Granada, Spain, September 16, 2018, Revised Selected Papers, Part II 4*, 311–320, Springer (2019).
- [6] Z. Jiang, C. Ding, M. Liu, *et al.*, “Two-stage cascaded u-net: 1st place solution to brats challenge 2019 segmentation task,” in *Brainlesion: Glioma, Multiple Sclerosis, Stroke and Traumatic Brain Injuries: 5th International Workshop, BrainLes 2019, Held in Conjunction with MICCAI 2019, Shenzhen, China, October 17, 2019, Revised Selected Papers, Part I 5*, 231–241, Springer (2020).
- [7] D. Zhang, G. Huang, Q. Zhang, *et al.*, “Cross-modality deep feature learning for brain tumor segmentation,” *Pattern Recognition* **110**, 107562 (2021).
- [8] J. Tsao, “Ultrafast imaging: principles, pitfalls, solutions, and applications,” *Journal of Magnetic Resonance Imaging* **32**(2), 252–266 (2010).
- [9] S. D. Serai, H. H. Hu, R. Ahmad, *et al.*, “Newly developed methods for reducing motion artifacts in pediatric abdominal mri: tips and pearls,” *American Journal of Roentgenology* **214**(5), 1042–1053 (2020).
- [10] D. Lee, J. Yoo, S. Tak, *et al.*, “Deep residual learning for accelerated mri using magnitude and phase networks,” *IEEE Transactions on Biomedical Engineering* **65**(9), 1985–1995 (2018).

- [11] Y. Huang, F. Zheng, R. Cong, *et al.*, “Mcmmt-gan: Multi-task coherent modality transferable gan for 3d brain image synthesis,” *IEEE Transactions on Image Processing* **29**, 8187–8198 (2020).
- [12] E. R. Chan, M. Monteiro, P. Kellnhofer, *et al.*, “pi-gan: Periodic implicit generative adversarial networks for 3d-aware image synthesis,” in *Proceedings of the IEEE/CVF conference on computer vision and pattern recognition*, 5799–5809 (2021).
- [13] X. Yi, E. Walia, and P. Babyn, “Generative adversarial network in medical imaging: A review,” *Medical image analysis* **58**, 101552 (2019).
- [14] J. Liu, A. I. Aviles-Rivero, H. Ji, *et al.*, “Rethinking medical image reconstruction via shape prior, going deeper and faster: Deep joint indirect registration and reconstruction,” *Medical Image Analysis* **68**, 101930 (2021).
- [15] K. Lei, M. Mardani, J. M. Pauly, *et al.*, “Wasserstein gans for mr imaging: from paired to unpaired training,” *IEEE transactions on medical imaging* **40**(1), 105–115 (2020).
- [16] J. J. Jeong, A. Tariq, T. Adejumo, *et al.*, “Systematic review of generative adversarial networks (gans) for medical image classification and segmentation,” *Journal of Digital Imaging* **35**(2), 137–152 (2022).
- [17] Z. Zhuang, Z. Yang, A. N. J. Raj, *et al.*, “Breast ultrasound tumor image classification using image decomposition and fusion based on adaptive multi-model spatial feature fusion,” *Computer methods and programs in biomedicine* **208**, 106221 (2021).
- [18] C. Han, L. Rundo, R. Araki, *et al.*, “Infinite brain mr images: Pggan-based data augmentation for tumor detection,” in *Neural approaches to dynamics of signal exchanges*, 291–303, Springer (2019).
- [19] N. Nahar, S. Soomro, and A. A. Monrat, “A gan based framework for multi-modal medical image segmentation,” (2021).
- [20] Z. Wang, Y. Zou, and P. X. Liu, “Hybrid dilation and attention residual u-net for medical image segmentation,” *Computers in biology and medicine* **134**, 104449 (2021).
- [21] Z. Huang, J. Zhang, Y. Zhang, *et al.*, “Du-gan: Generative adversarial networks with dual-domain u-net-based discriminators for low-dose ct denoising,” *IEEE Transactions on Instrumentation and Measurement* **71**, 1–12 (2021).
- [22] K. Armanious, C. Jiang, M. Fischer, *et al.*, “Medgan: Medical image translation using gans,” *Computerized medical imaging and graphics* **79**, 101684 (2020).
- [23] P. Isola, J.-Y. Zhu, T. Zhou, *et al.*, “Image-to-image translation with conditional adversarial networks,” in *Proceedings of the IEEE conference on computer vision and pattern recognition*, 1125–1134 (2017).
- [24] J.-Y. Zhu, T. Park, P. Isola, *et al.*, “Unpaired image-to-image translation using cycle-consistent adversarial networks,” in *Proceedings of the IEEE international conference on computer vision*, 2223–2232 (2017).
- [25] B. Yu, L. Zhou, L. Wang, *et al.*, “3d cgan based cross-modality mr image synthesis for brain tumor segmentation,” in *2018 IEEE 15th international symposium on biomedical imaging (ISBI 2018)*, 626–630, IEEE (2018).

- [26] B. Yu, L. Zhou, L. Wang, *et al.*, “Ea-gans: edge-aware generative adversarial networks for cross-modality mr image synthesis,” *IEEE transactions on medical imaging* **38**(7), 1750–1762 (2019).
- [27] E. Jung, M. Luna, and S. H. Park, “Conditional gan with an attention-based generator and a 3d discriminator for 3d medical image generation,” in *Medical Image Computing and Computer Assisted Intervention–MICCAI 2021: 24th International Conference, Strasbourg, France, September 27–October 1, 2021, Proceedings, Part VI* **24**, 318–328, Springer (2021).
- [28] J. M. Wolterink, A. M. Dinkla, M. H. Savenije, *et al.*, “Deep mr to ct synthesis using unpaired data,” in *Simulation and Synthesis in Medical Imaging: Second International Workshop, SASHIMI 2017, Held in Conjunction with MICCAI 2017, Québec City, QC, Canada, September 10, 2017, Proceedings 2*, 14–23, Springer (2017).
- [29] J. P. Cohen, M. Luck, and S. Honari, “Distribution matching losses can hallucinate features in medical image translation,” in *Medical Image Computing and Computer Assisted Intervention–MICCAI 2018: 21st International Conference, Granada, Spain, September 16–20, 2018, Proceedings, Part I*, 529–536, Springer (2018).
- [30] Y. Hiasa, Y. Otake, M. Takao, *et al.*, “Cross-modality image synthesis from unpaired data using cyclegan: Effects of gradient consistency loss and training data size,” in *Simulation and Synthesis in Medical Imaging: Third International Workshop, SASHIMI 2018, Held in Conjunction with MICCAI 2018, Granada, Spain, September 16, 2018, Proceedings 3*, 31–41, Springer (2018).
- [31] M. Arjovsky, S. Chintala, and L. Bottou, “Wasserstein generative adversarial networks,” in *International conference on machine learning*, 214–223, PMLR (2017).
- [32] L. Fidon, S. Ourselin, and T. Vercauteren, “Generalized wasserstein dice score, distributionally robust deep learning, and ranger for brain tumor segmentation: Brats 2020 challenge,” in *Brainlesion: Glioma, Multiple Sclerosis, Stroke and Traumatic Brain Injuries: 6th International Workshop, BrainLes 2020, Held in Conjunction with MICCAI 2020, Lima, Peru, October 4, 2020, Revised Selected Papers, Part II* **6**, 200–214, Springer (2021).
- [33] Q. Hou, D. Zhou, and J. Feng, “Coordinate attention for efficient mobile network design,” in *Proceedings of the IEEE/CVF conference on computer vision and pattern recognition*, 13713–13722 (2021).
- [34] S. Woo, J. Park, J.-Y. Lee, *et al.*, “Cbam: Convolutional block attention module,” in *Proceedings of the European conference on computer vision (ECCV)*, 3–19 (2018).
- [35] D. P. Kingma and J. Ba, “Adam: A method for stochastic optimization,” *arXiv preprint arXiv:1412.6980* (2014).
- [36] T. Kim, M. Cha, H. Kim, *et al.*, “Learning to discover cross-domain relations with generative adversarial networks,” in *International conference on machine learning*, 1857–1865, PMLR (2017).
- [37] M.-Y. Liu, T. Breuel, and J. Kautz, “Unsupervised image-to-image translation networks,” *Advances in neural information processing systems* **30** (2017).
- [38] S. U. Dar, M. Yurt, L. Karacan, *et al.*, “Image synthesis in multi-contrast mri with conditional generative adversarial networks,” *IEEE transactions on medical imaging* **38**(10), 2375–2388 (2019).

- [39] A. Hore and D. Ziou, “Image quality metrics: Psnr vs. ssim,” in *2010 20th international conference on pattern recognition*, 2366–2369, IEEE (2010).
- [40] O. Ronneberger, P. Fischer, and T. Brox, “U-net: Convolutional networks for biomedical image segmentation,” in *Medical Image Computing and Computer-Assisted Intervention–MICCAI 2015: 18th International Conference, Munich, Germany, October 5-9, 2015, Proceedings, Part III 18*, 234–241, Springer (2015).
- [41] F. Isensee, P. F. Jaeger, S. A. Kohl, *et al.*, “nnu-net: a self-configuring method for deep learning-based biomedical image segmentation,” *Nature methods* **18**(2), 203–211 (2021).
- [42] D. G. Ellis and M. R. Aizenberg, “Deep learning using augmentation via registration: 1st place solution to the autoimplant 2020 challenge,” in *Towards the Automatization of Cranial Implant Design in Cranioplasty: First Challenge, AutoImplant 2020, Held in Conjunction with MICCAI 2020, Lima, Peru, October 8, 2020, Proceedings 1*, 47–55, Springer (2020).